Nabutola and Boetcher *Advances in Aerodynamics* (2021) 3:29
https://doi.org/10.1186/s42774-021-00086-7

Advances in Aerodynamics

RESEARCH Open Access

Assessment of conventional and air-jet wheel deflectors for drag reduction of the DrivAer model

Kaloki L. Nabutola and Sandra K. S. Boetcher*

*Correspondence:
sandra.boetcher@erau.edu
Department of Mechanical Engineering, Embry-Riddle Aeronautical University, Daytona Beach, FL, USA

Abstract

Aerodynamic drag is a large resistance force to vehicle motion, particularly at highway speeds. Conventional wheel deflectors were designed to reduce the wheel drag and, consequently, the overall vehicle drag; however, they may actually be detrimental to vehicle aerodynamics in modern designs. In the present study, computational fluid dynamics simulations were conducted on the notchback DrivAer model—a simplified, yet realistic, open-source vehicle model that incorporates features of a modern passenger vehicle. Conventional and air-jet wheel deflectors upstream of the front wheels were introduced to assess the effect of underbody-flow deflection on the vehicle drag. Conventional wheel-deflector designs with varying heights were observed and compared to 45° and 90° air-jet wheel deflectors. The conventional wheel deflectors reduced wheel drag but resulted in an overall drag increase of up to 10%. For the cases studied, the 90° air jet did not reduce the overall drag compared to the baseline case; the 45° air jet presented drag benefits of up to 1.5% at 35 m/s and above. Compared to conventional wheel deflectors, air-jet wheel deflectors have the potential to reduce vehicle drag to a greater extent and present the benefit of being turned off at lower speeds when flow deflection is undesirable, thus improving efficiency and reducing emissions.

Keywords: Vehicle aerodynamics, Wheel and wheelhouse aerodynamics, Automotive, Active flow control, Passive flow control, DrivAer

1 Introduction

In the last few decades, numerous vehicle models have been developed to study the flow field around various features of ground vehicles. Le Good and Garry [1] designate vehicle models by three categories: simple bodies, basic car shapes, and series cars (which are based on production vehicles). The Ahmed body is an example of a simple body that was developed in the 1980s to study the wake region created by a slant, such as that seen in the C-pillar of production vehicles [2]. The SAE reference model, also known as the Pininfarina model, is an example of a basic car shape that was designed to study the effects of varying ride height [3]. The SAE model is more geometrically complex than the Ahmed body, but provides relatively simplistic insight on the flow field around a ground vehicle.

Springer Open

© The Author(s). 2021 **Open Access** This article is licensed under a Creative Commons Attribution 4.0 International License, which permits use, sharing, adaptation, distribution and reproduction in any medium or format, as long as you give appropriate credit to the original author(s) and the source, provide a link to the Creative Commons licence, and indicate if changes were made. The images or other third party material in this article are included in the article's Creative Commons licence, unless indicated otherwise in a credit line to the material. If material is not included in the article's Creative Commons licence and your intended use is not permitted by statutory regulation or exceeds the permitted use, you will need to obtain permission directly from the copyright holder. To view a copy of this licence, visit http://creativecommons.org/licenses/by/4.0/.

The study of simple bodies and basic car shapes is useful in initial parametric studies but often presents limitations in terms of transitioning to practical applications due to a lack of true resemblance to modern passenger cars. The DrivAer model, developed by Technische Universität München (TUM) in conjunction with BMW and Audi, is a combination of the Audi A4 and a 3-series BMW and is a better representation of a realistic passenger vehicle compared to other simplified generic models, such as the Ahmed body [4]. The DrivAer model is a modular package which allows the user to choose between a fastback, notchback, or estateback configuration with a number of other features such as the inclusion of an engine bay, side mirrors, detailed underbody, detailed wheels, and an exhaust system. In addition to introducing the model, Heft et al. [4] presented experimental data on the drag coefficient experienced by different configurations of the DrivAer model, with and without ground simulation, as well as the pressure distribution along the midplane of the body.

The DrivAer model, an open-source geometry, has gained popularity in recent years due to an abundant amount of available experimental data for model validation. Wind tunnel experiments have been conducted by Strangfeld et al. [5] on the fastback DrivAer model to determine the lift, drag, and side forces using a 6-component force balance and to visualize the flow field using pressure probes and particle image velocimetry (PIV). Wieser et al. [6] conducted similar experimental work comparing the flow field of the fastback and notchback DrivAer configurations with an applied sidewind using 25% scale models mounted in a wind tunnel. Studies of flow-control devices on the more realistic DrivAer reference model have been used to relate findings based on simplified vehicle models, such as the Ahmed body, to production cars. Wieser et al. [7] investigated the effects of triangular and circular vortex generators on the notchback DrivAer model using wind tunnel experiments. Although a previous study showed that vortex generators are beneficial for the Ahmed body [8], Wieser et al. [7] found that their use on the notchback DrivAer model came with a larger drag penalty than drag reduction.

Flow-control devices, which can either be passive or active, are generally implemented on production and performance vehicles to reduce drag or to increase downforce [9–12]. Aerodynamic drag is the dominant resistive force for passenger cars traveling on the highway, and about 50% of the engine power is used to overcome this force [13]. For a road vehicle, pressure drag dominates while friction drag forms a smaller portion of the total aerodynamic drag [14]. A reduction in aerodynamic drag leads to better fuel efficiency, which is a very desirable outcome in present-day engineering when strict regulations are being imposed for automotive manufacturers globally due to environmental concerns. Additionally, an improvement in fuel efficiency is beneficial because it leads to lower fuel expenses. Many small improvements to the aerodynamics of a vehicle could add up to a substantial gain, and there have been some particular areas that have been deemed suitable candidates for drag-reduction opportunities. The wheelhouse region contributes 25-30% of the overall drag of a passenger vehicle [15], a significant portion, making this region a suitable candidate for a drag-reduction opportunity.

One commonly used passive flow-control device is a wheel deflector which is placed upstream of a rotating wheel, causing incoming flow to yaw prior to reaching the wheel and thereby altering the stagnation point of flow on the wheel. Sebben [16] conducted numerical simulations of a detailed vehicle geometry fitted with various front-wheel-deflector designs to assess the impact on the drag coefficient. Some designs were found

to reduce the overall drag of the vehicle by reducing the drag contribution of the wheel, while other designs did not successfully cause a drag reduction. Sebben [16] concluded that while wheel deflectors had the potential of reducing the drag of a vehicle by up to 10 drag counts, they had to be carefully designed and placed in order to have a net-positive effect. Front-wheel deflectors have since been studied in more detail and incorporated in many vehicle designs. The Nissan Qashqai, for example, is a crossover SUV that benefits greatly from front-wheel deflectors that cause an overall drag reduction of $\sim 6\%$ [17].

Although requiring additional energy expenditures, a number of experimental [18–21] and numerical [22, 23] studies have shown promising results using active flow control, in the form of jets, to reduce drag by modifying the wake region of simplified automotive bodies. For example, a study by Barsotti et al. [22] on controlling the wake region of an Ahmed body using wall jets showed that the overall drag of the bluff body can be reduced by up to 22%. Fewer studies have been performed to investigate active flow control on more realistic bodies. Baek and Lee [24] performed a numerical study to investigate the effects of continuous blowing from slots located at the end of the roof and at the C-pillar of DrivAer models with various backs. From the cases simulated, they found a maximum drag reduction of 7.5%. Wieser et al. [25] performed an experimental study to examine the effect of fluid oscillators on the aerodynamic coefficients of the notchback DrivAer model with a smooth underbody. They found that the actuation resulted in a net-drag decrease of around 3.5%, thus demonstrating the potential for oscillating jets to influence the aerodynamic behavior.

Recently, active flow control has been applied to modify the flow in and around the wheelhouse for a simplified body with the intent of reducing overall vehicle drag. Since many simplified bodies, such as the Ahmed body, lack rotating wheels, Fabijanic [26] developed a two-wheeled bluff body for the purpose of investigating the wheelhouse air flow. Active flow control has been simulated on the Fabijanic body in the form of air-jet wheel deflectors. Lee [27] found that the use of air jets upstream of the wheelhouse reduced the overall drag coefficient of the simplified body by changing the momentum of the incoming flow without an additional drag-inducing surface, as is the case with conventional wheel deflectors. Nabutola and Boetcher [28] found that a wheel-drag reduction of 16% could be achieved using air-jet wheel deflectors, which corresponded to an overall drag reduction of 2.8% for the Fabijanic body. Air-jet wheel deflectors have the potential to greatly impact the drag of modern passenger cars where the wheel drag is a more substantial portion of the overall drag compared to the Fabijanic body.

The present study includes an assessment of conventional and air-jet wheel deflectors for reducing the drag of the notchback DrivAer reference model. Prior to introducing flow-modification devices, a series of transient simulations, using multiple turbulence-modeling approaches, was first conducted to compare their performance and computational cost for the baseline model. Based on the results of the baseline simulations, wall-modeled large eddy simulation (WMLES) was chosen as the turbulence model for the simulations involving flow-modification devices. The height of the conventional wheel deflectors and the velocity of the air-jet wheel deflectors were parametrically varied. The results show the opportunity for drag reduction using air-jet wheel deflectors at higher speeds.

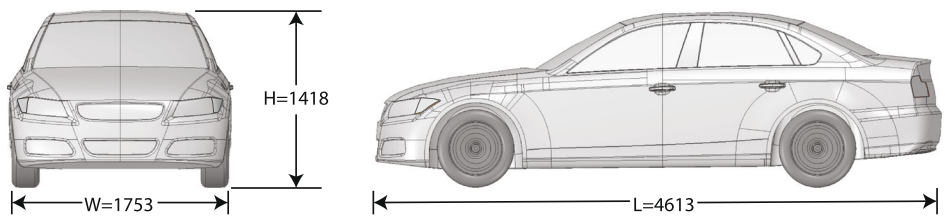

Fig. 1 Notchback DrivAer model with simplified underbody, closed wheels, and no mirrors (dimensions in mm)

2 Physical model

A full-scale notchback DrivAer reference model, with a smooth underbody, closed engine bay, closed wheels, and no side mirrors, was analyzed in the present investigation. The overall dimensions of the vehicle model are shown in Fig. 1. The configuration for the present investigation was judiciously chosen to minimize computational cost while focusing on the areas that would be most impacted by the presence of the flow-modification devices being studied. While the side mirrors are not an insignificant source of drag on the vehicle model, their inclusion would not offer further insight on the influence of the wheel deflectors. However, including them means solving another unsteady wake region which would require mesh refinement in their vicinity—further increasing the number of cells to resolve details in the flow field that are not critical to the present study.

The closed-wheel configuration was chosen because the largest source of drag experienced by the vehicle model is pressure drag. The sidewall contribution of the closed wheel to the pressure drag is negligible compared to the pressure drag that results from the underbody flow that impacts the front of the wheels. Additionally, including the detailed rim would require an unsteady sliding mesh that accounts for the position of the rim spokes with time. This would add significant computational time due to an increase in the number of cells and time-dependent remeshing. The closed rim provides a good first approximation as to whether these devices are effective. However, there are additional considerations that future work will address. The use of a detailed rim will provide more understanding of the "fan effect" on the flow field that results from the flow-modification devices. The fan moment, first documented by Wickern et al. [15], is a phenomenon that results from a combination of offset resultant aerodynamic force on the wheel, rotational component of flow imparted by the rotating motion of the spokes, and the frictional force on the rotating wheel caused by the shear stress associated with the oncoming flow field.

2.1 Conventional wheel deflectors

Sebben [16] conducted numerical and experimental work of several conventional wheel-deflector designs on a simplified vehicle body and observed a drag reduction with almost all designs considered—some designs being significantly more effective than others. Sebben [16] applied a steady-state approach in order to reduce computational cost, even though the flow field within the wheelhouse and in the wake of a ground vehicle is largely unstable.

Three different conventional wheel-deflector designs were applied to the notchback DrivAer reference model. The designs were similar to those that [16] reported to produce the greatest drag reduction. All wheel deflectors were designed to conform with the end

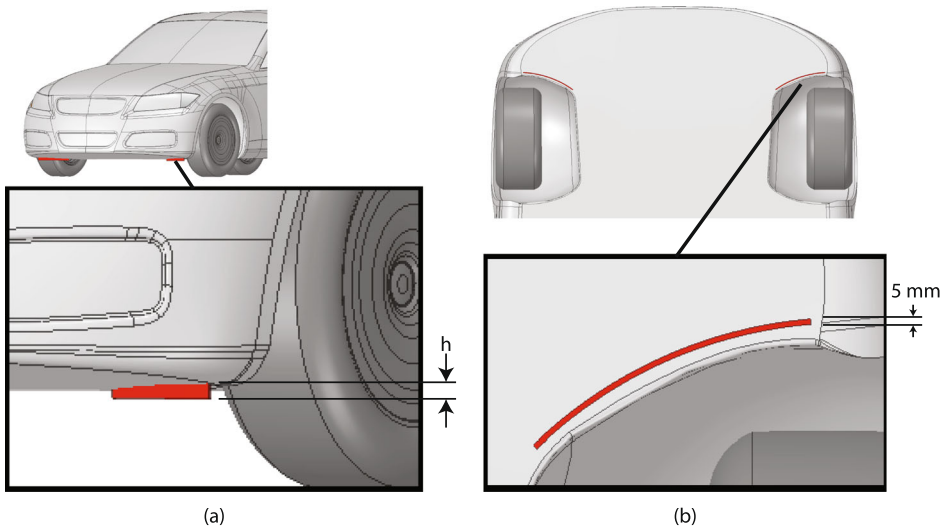

Fig. 2 Notchback DrivAer model with a conventional wheel deflector (**a**) front view and (**b**) bottom view

curvature of the wheelhouse as shown in Fig. 2. The wheel deflectors have a total length of 268 mm and a thickness of 5 mm. The short, medium, and long wheel deflectors have heights of h = 15, 25, and 50 mm, respectively.

2.2 Air-jet wheel deflectors

Two different air-jet wheel deflector designs were analyzed. The profile of the first air-jet wheel deflector was similar to the conventional wheel deflector and spanned the front curvature of the wheelhouse. The air jets, shown in Fig. 3, were aimed perpendicular (90°) to the incoming underbody flow with the intention of causing air deflection similar to the conventional wheel deflector. A second design that was intended to cause smoother mixing of the jet stream and underbody flow was also investigated. In this design, which is

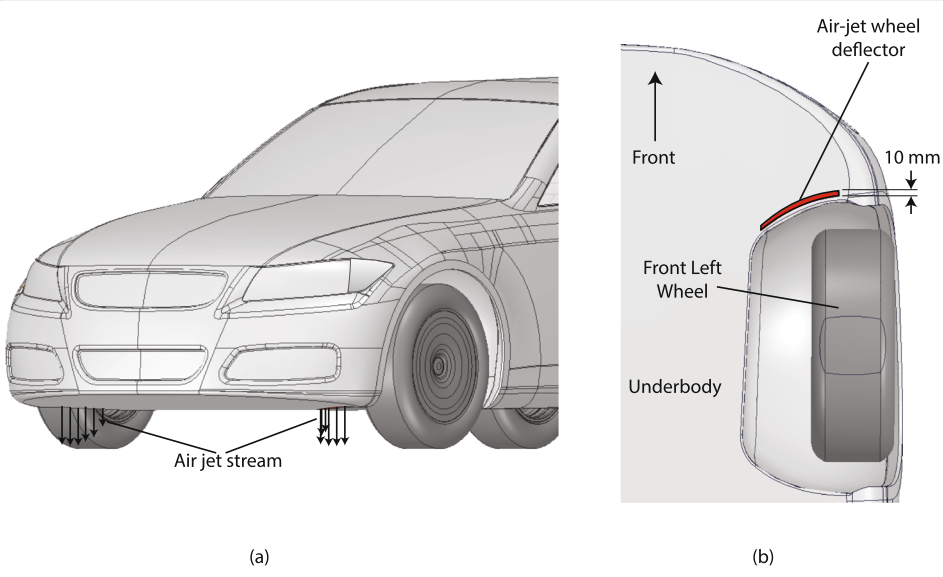

Fig. 3 Notchback DrivAer model with a 90° air-jet wheel deflector (**a**) front view and (**b**) bottom view

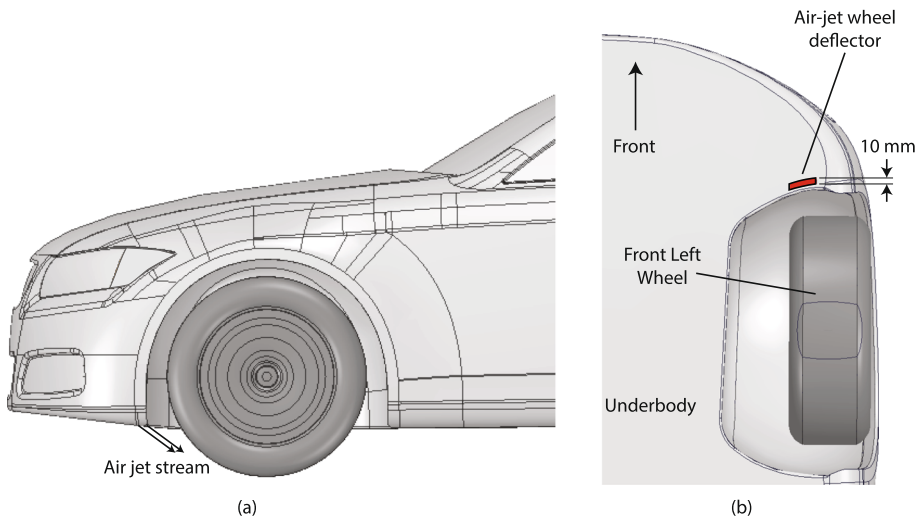

Fig. 4 Notchback DrivAer model with a 45° air-jet wheel deflector (**a**) side view and (**b**) bottom view

shown in Fig. 4, the jet stream only spanned the portion of the wheelhouse that overlapped with the front wheels and was angled at 45° to the underbody flow.

3 Turbulence models

The flow around the DrivAer model is incompressible, subsonic, and turbulent. Three turbulence models were investigated to determine a suitable model for evaluating the flow-modification devices: shear-stress transport (SST) k-ω, improved delayed detached eddy simulation (IDDES), and WMLES. The SST k-ω turbulence model [29, 30] has been shown to work well for simulating flow separation where there is an adverse pressure gradient. Other authors [31] have found excellent agreement with experimental results for the DrivAer model using the scale-adaptive simulation (SAS) model [32]. The use of Reynolds-averaged Navier-Stokes (RANS) sacrifices a portion of the true physics of the flow through the averaging process. This is beneficial because it allows the mesh resolution to be coarser since the flow is not being fully resolved. However, for a more realistic representation of the flow field, flow-resolving eddy-viscosity models such as large eddy simulation (LES) and detached eddy simulation (DES) should be implemented. Both methods have much more stringent spatial and temporal discretization requirements and, therefore, require more computational resources.

Ashton and Revell [33] compared the use of RANS and DES in simulating the flow around the DrivAer reference model and validated their results using forces and pressure coefficients determined experimentally. The authors found that DES produced more accurate results than various turbulence models assessed, including the one-equation Spalart-Allmaras model and the more commonly used realizable k-ϵ and SST k-ω models. Choi et al. [34] compared the performance of the SST k-ω model and IDDES [35] on determining the flow field around the DrivAer model. The authors found that a transient analysis using IDDES produced a drag coefficient more consistent with experimental results. Ajure et al. [36] compared the results obtained using classic LES and WMLES on numerical simulations of a fastback DrivAer model. The authors found that a 70% reduction in computational time was achieved using WMLES instead of classic LES.

To the best knowledge of the authors, no prior investigators have performed a detailed turbulence-model validation for flow within the wheelhouse of a DrivAer model. Collin et al. [37] provide overall wheel drag coefficients separate from the main body with comparison to CFD; however, the results presented do not differentiate between front and rear wheels, and wheel pressure coefficient distributions are not provided. Nonetheless, previous work has been done to investigate LES models for flow around a wheel in a wheelhouse for a Fabijanic body. Krajnović et al. [38] used LES to investigate its efficacy in modeling the drag and surface pressure coefficients of the wheel and wheelhouse of a Fabijanic body. They reported that even though the difference between the drag coefficients determined from LES and the experimental data was between 20 and 30%, they noted that the experimental uncertainty of the Fabijanic [26] results was quite high—between 20 and 35%. Nabutola and Boetcher [39] recently evaluated several different turbulence models, including IDDES and WMLES, for flow around a wheel and wheelhouse for a Fabijanic body. The difference in the simulated time-averaged wheel drag coefficients for IDDES and WMLES was 0.3%. The values for IDDES and WMLES were slightly outside the lower bound of the Fabijanic experimental uncertainty by approximately 1%. In regards to surface pressure coefficients within the wheelhouse, the nearly identical IDDES and WMLES values agreed the most with the Fabijanic data. Although some discrepancies existed, general trends were on par with the experimental data. Both Krajnović et al. [38] and Nabutola and Boetcher [39] discuss the issues related to the Fabijanic experiment and reasons for discrepancies. Based on this information, the accuracy and computational time of IDDES and WMLES in modeling the DrivAer model are further investigated in the present study.

4 Spatial and temporal discretization

Fluent meshing was used to create three different meshes for the full-scale baseline model. In all cases, the cells in the freestream were sized at 300 mm. Advanced cell-sizing features were used to ensure that curvature was captured for the wheels and the DrivAer walls in order to accurately represent the geometry. Prismatic cells extruded from the walls of the DrivAer body and the wheels were used to control the near-wall mesh density in order to resolve the boundary layer and accurately determine the aerodynamic coefficients. A portion of the wheel was truncated to create a contact patch where the wheel meets the ground in order to prevent tangency which would otherwise present problems with meshing. In reality, tangency with the ground does not occur at a point because the wheel deforms near the ground due to the weight of the vehicle. Cells were concentrated near the contact patch to capture the large pressure and velocity gradients that exist in that region.

For flow-resolving methods such as LES, there are stringent grid requirements for the streamwise, wall-normal, and spanwise cell dimensions. Best practices recommend that $\Delta x^+ \approx 100$, $y^+ \approx 1$, and $\Delta z^+ \approx 30$ [40]. The coarse mesh was designed to meet these cell-sizing recommendations; the medium and fine meshes were further refinements of the coarse mesh. Bodies of influence were used to control the maximum cell size near the DrivAer walls and, even more so, within the wheelhouse region to ensure that turbulent flow structures were accurately resolved. Table 1 summarizes the mesh-sizing details. Figure 5 shows the surface mesh for the coarse mesh along with a part of the mesh at the midplane of the solution domain with a close-up of the near-wall resolution.

Table 1 Mesh and time-step details

	Coarse	Medium	Fine
Minimum Cell Size (mm)	2.00	1.75	1.50
First-Cell Height (mm)	0.020	0.017	0.016
Number of Layers	20	25	25
Average Wall y+	0.36	0.30	0.28
Average Δ x+	30	26	21
Average Δ z+	30	26	21
Number of Cells (million)	34	50	60
Time-Step Size (s)	5×10^{-5}	4×10^{-5}	3.5×10^{-5}

The numerical simulations were conducted for a physical time of 1 s, which corresponds to 16 wheel revolutions for the 15 m/s cases. For each time step, the criteria for convergence was set to 1×10^{-5} for the continuity, momentum, and turbulence equations. The Courant-Friedrichs-Lewy (CFL) number is used to determine stability, particularly with explicit temporal schemes. A larger time step requires less computational resources to simulate a specified physical time but may not sufficiently resolve time scales. Ekman et al. [41] conducted studies on the accuracy of scale-resolving simulations with various time-step sizes on the DrivAer reference model. The authors found that significant savings in computational time were achieved with sufficiently accurate results up to a CFL of 20; however, as the time-step size increased, larger discrepancies were seen at the A-pillar, side window, C-pillar, and the wheels. Accurately representing the flow, particularly

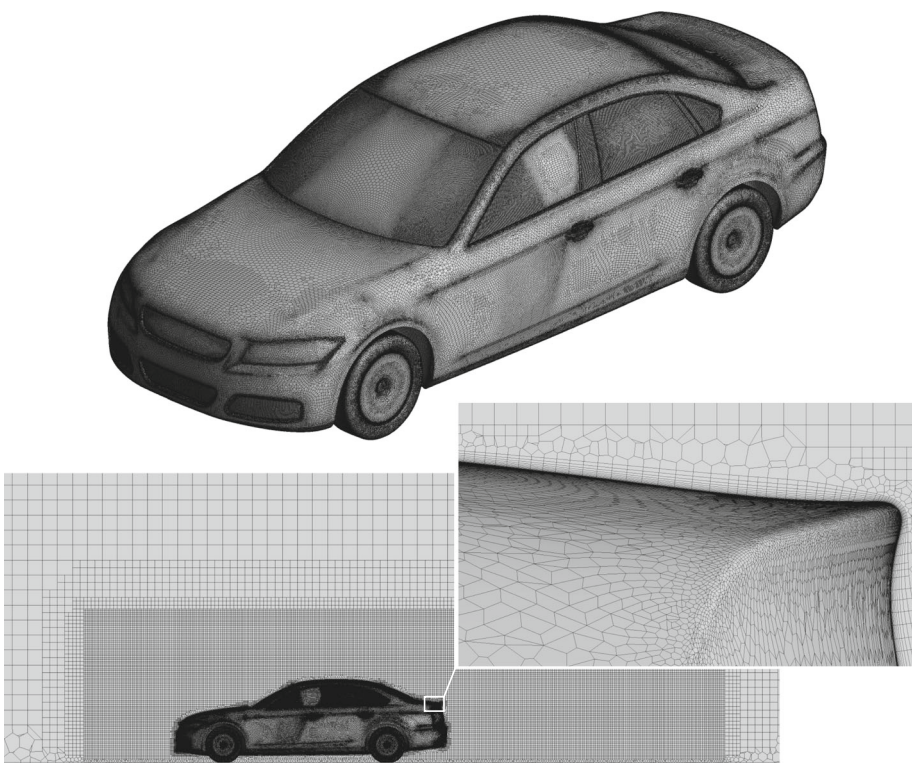

Fig. 5 Surface mesh of the notchback DrivAer model and mid-plane mesh with close-up of the boundary layer

in the wheelhouse region, was deemed important in this study; therefore, a time step was chosen such that a CFL of unity for most of the solution domain was achieved.

$$CFL = \frac{U_\infty \Delta t}{\Delta x} \tag{1}$$

Here, U_∞ is the wind tunnel inlet velocity, Δx is the length interval, and Δt is the time step.

5 Numerical solver and boundary conditions

Fluent 19.2 was used to conduct all CFD simulations of the DrivAer model. All transient simulations were initiated from a converged steady-state solution using the SST k-ω turbulence model. Second-order formulation was used for discretization of pressure, turbulence kinetic energy, and specific dissipation rate. Second-order implicit transient formulation was applied with warped-face gradient correction. Bounded central difference was applied for the momentum formulation, as is recommended for LES and DES due to its low numerical dissipation. The pressure-velocity coupling applied for all cases was a semi-implicit method for pressure linked equations-consistent (SIMPLEC).

The solution domain is shown in Fig. 6. An inlet velocity is specified five car-lengths upstream of the DrivAer model. A moving ground plane having the same translational velocity as the inlet velocity was applied. Twelve car-lengths downstream, an outlet with 0 Pa gauge pressure was specified. A symmetry boundary condition which specifies zero flux of all quantities was applied to all other boundaries of the fluid enclosure.

An initial freestream velocity of 15 m/s was chosen for model validation using wind tunnel experiments conducted by Heft et al. [4] on the baseline notchback DrivAer model. The open-road configuration is commonly used as an analog comparing wind tunnel tests

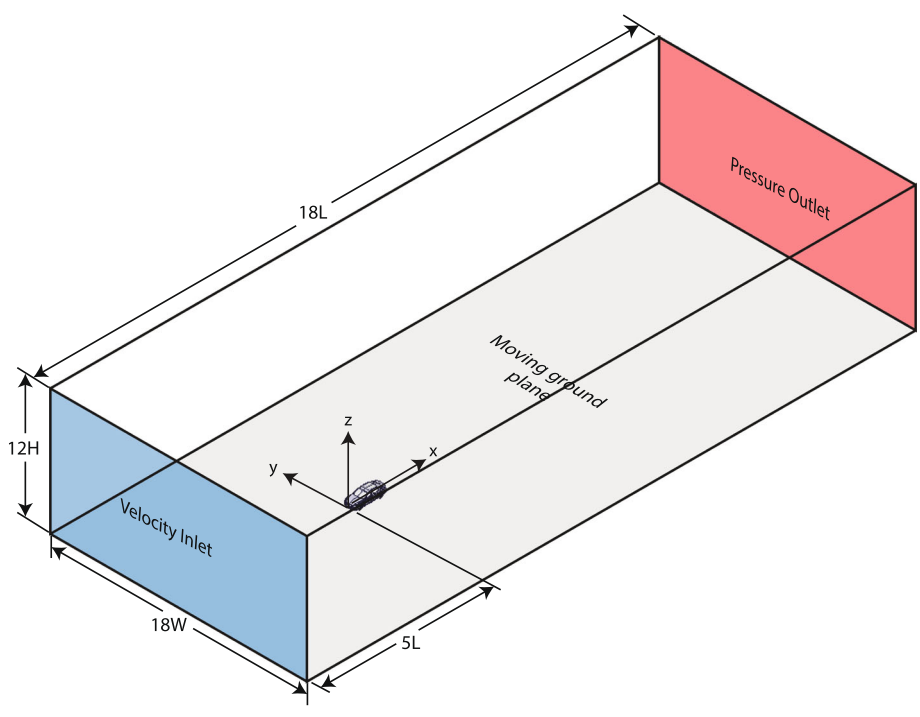

Fig. 6 Solution domain and boundary conditions

to more realistic driving conditions. Modern wind tunnels are capable of achieving inlet turbulence intensities of 0.5%. However, since the geometry used in the present investigation is based on an open-road configuration, a turbulence intensity of 5% was specified at the inlet. Furthermore, a turbulent viscosity ratio of 10 was also specified. The vehicle model was placed sufficiently far downstream of the inlet to minimize solution sensitivity to the inlet conditions. The Reynolds number is defined as

$$Re = \frac{\rho U_\infty L}{\mu} \tag{2}$$

A Reynolds number of 4.66×10^6 was calculated using a velocity of 15 m/s and a reference length, L, of 4.62 m—the length of the full-scale DrivAer model. Standard air properties were used to determine the density, ρ, and the dynamic viscosity, μ.

Flow-modification devices were assessed for a range of vehicle speeds. A speed of 15 m/s (34 mph) was used for Reynolds-number matching with the original DrivAer experiments [4] and to assess the effectiveness of the flow-modification devices. Additional tunnel inlet speeds of 25 m/s (56 mph), 35 m/s (78 mph), and 45 m/s (100 mph) were also investigated because they are more representative of highway speeds where aerodynamic drag is the dominant resistance to ground-vehicle motion.

The closed-wheel geometry excludes the rim spokes; therefore, there are flow structures associated with the spinning rims that are not accounted for by the current model. However, the tangent-velocity approach has been found to produce results that are in agreement with experimentation without the need for time-dependent remeshing, which leads to a major saving in computational time [42]. Therefore, a rotating-wall boundary condition was applied to the wheels such that the tangential component at the contact between the wheel and the ground would be equal to the forward motion of the vehicle.

Conventional wheel deflectors were realized with a geometry variation; air-jet wheel deflectors were implemented using a velocity inlet. The speed of air injection, U_{jet}, was varied parametrically, and the impact on wheel drag and overall drag of the vehicle model was assessed. In the following equation, the jet speed was non-dimensionalized using the freestream air speed, varied in increments of U = 1/3.

$$U = \frac{U_{jet}}{U_\infty} \qquad 1/3 \le U \le 6/3 \tag{3}$$

6 Baseline model and turbulence model validation

6.1 Drag coefficient

The original experimental DrivAer work was conducted by Heft et al. [4] on a 40% scale version of the model. The experiments of [4] include the configuration studied here (notchback, smooth underbody, no side mirrors, and ground simulation). Collin et al. [37] conducted both numerical (full-scale) and experimental (40% scale) studies on the DrivAer model with the various backs installed. Although they investigated the notchback DrivAer model with a smooth underbody and ground simulation, they included the mirrors, which, according to the results of [4], can add more than 10 counts of drag to the overall vehicle drag coefficient. Additional detailed experimental results for full-scale models of the DrivAer body tested in several different wind tunnel facilities are provided by James et al. [43]. However, the results presented by [43] for smooth-underbody configurations were obtained using static ground and not a moving belt system. Therefore, the aerodynamic drag simulated by the three meshes in the present study was compared to

Table 2 Overall drag coefficients from CFD compared to experimental data for the baseline model

Turbulence Model/Experiment	Coarse	Medium	Fine	Experiment
SST k-ω - Steady	0.242	0.245	0.242	
IDDES - Transient	0.242	0.242	0.234	
WMLES - Transient	0.231	0.240	0.227	
Heft et al. [4]				0.232

[4] for a notchback DrivAer model with moving wheels, a simplified underbody, and no side mirrors. The drag coefficient is defined as

$$C_D = \frac{F_x}{\frac{1}{2}\rho U_\infty^2 A_F} \tag{4}$$

In this equation, F_x is the total drag force, composed of both pressure and friction drag and A_F = 2.11 m^2—the frontal area of the vehicle model.

Table 2 compares the total, time-averaged drag coefficients obtained using CFD with the experimental results [4]. The drag coefficients obtained after the initial steady SST k-ω analysis deviated the most from Heft et al. [4]. Soares and de Souza [42] assessed the performance of various RANS models in determining the aerodynamic forces experienced by the fastback DrivAer model at two different speeds: 16 m/s and 40 m/s. Among the RANS models assessed, they found that the drag coefficient determined by the SST k-ω model deviated 19% from the experimental value. However, these authors found that the realizable k-ϵ model agreed better with the experimental data than the SST k-ω model at both speeds (<2%). Regardless, due to the unsteady nature of the flow, using a steady-state solver can lead to inaccurate results. Additionally, the development of flow structures in the inherently unsteady regions will not be captured accurately—hence the need for flow-resolving techniques.

Flow-resolving methods produced results that were more consistent with the experiment, where WMLES matched the experimental data better than IDDES. Based on these results, WMLES with the coarse mesh was used for the passive and active flow-control studies presented here. Further validation of WMLES with the coarse mesh is presented in the lift and pressure coefficient sections. The present results are on the same order of accuracy as those by Collin et al. [37], who used delayed detached eddy simulation (DDES) on a full-scale notchback DrivAer model with the same configuration as the present investigation with the exception that they included the side mirrors. Additionally, [37] conducted CFD simulations with and without the top strut used to keep the vehicle model in position in the wind tunnel. With the strut modeled, their average numerical drag coefficient was 3.7% different from the same corresponding configuration (considering side mirrors) from Heft et al. [4]; without the strut, their numerical drag coefficient was <1% from Heft's wind tunnel experiments.

6.2 Lift coefficient

The lift coefficient is defined as

$$C_L = \frac{F_z}{\frac{1}{2}\rho U_\infty^2 A_F} \tag{5}$$

Here, F_z is the lift force.

The lift coefficient determined from the WMLES with the coarse mesh in the present study is 0.0232, which translates into a lift-to-drag ratio of 0.1. The lift coefficient, in general, is challenging to validate. Heft et al. [4] focused on the drag and pressure coefficients, but neglected to present any results on lift coefficients. To the best knowledge of the authors, there is no published experimental data for the lift coefficient for a notchback DrivAer model with no side mirrors, smooth underbody, and ground simulation.

Numerical studies of ground vehicles are often performed in an open-road setting to simulate more realistic vehicle operation. While there is good agreement between wind tunnel experiments and numerical simulations for the drag coefficient, there are still disparities for the lift coefficient despite correction factors that account for blockage, ground effects, and wall effects [44]. A wide-range of lift coefficient values for other configurations of the notchback DrivAer model are seen in the experimental literature. Collin et al. [37] present inconsistent lift coefficient results for the notchback DrivAer model with mirrors, smooth underbody, and moving wheels for two wind tunnel facilities: TUM (Munich, Germany) (C_L = -0.028) and Audi (Ingolstadt, Germany) (C_L = 0.004). James et al. [43] experimentally determined a lift coefficient of 0.031 for a notchback DrivAer model without mirrors, smooth underbody, and static ground.

6.3 Pressure coefficient

Surface pressure coefficients were compared to experimental data that was obtained using pressure probes on the surface of the DrivAer reference model along the midline of the upperbody and the underbody. The pressure coefficient is defined as

$$C_P = \frac{p - p_\infty}{\frac{1}{2}\rho U_\infty^2} \tag{6}$$

In this equation, p is the pressure and p_∞ is the freestream pressure.

Figure 7(a) shows the upperbody pressure coefficient compared to experimental data from [4] and [43]. James et al. [43] conducted wind tunnel tests to determine surface pressure data for only a detailed underbody at three different locations: Monash University (Clayton, Australia), Tongji University (Shanghai, China), and PVT (Gothenburg, Sweden). Heft et al. [4] observed very minute differences in the pressure coefficients of the upperbody between the smooth and detailed underbody, as well as with and without ground simulation. Therefore, it is appropriate to compare the upperbody pressure coefficients for a smooth underbody, obtained using CFD, to experimental work conducted with a detailed underbody. Surface pressure data is shown here for WMLES with the coarse mesh (which adequately predicted the drag coefficient) for further validation of the baseline case.

Generally, there is good agreement between the pressure coefficients obtained numerically with the coarse mesh and the experimental results used for comparison. As seen in Fig. 7(a), there are a few regions of discrepancy, some of which can be attributed to the low resolution of pressure probes used during the wind tunnel tests. Pressure coefficients obtained numerically are much lower than the experimental results in region A. This is because there are large surface pressure gradients near the front of the vehicle that are not adequately captured experimentally due to too few pressure probes. However, wind tunnel experiments conducted at PVT are shown to capture a lower pressure in region A,

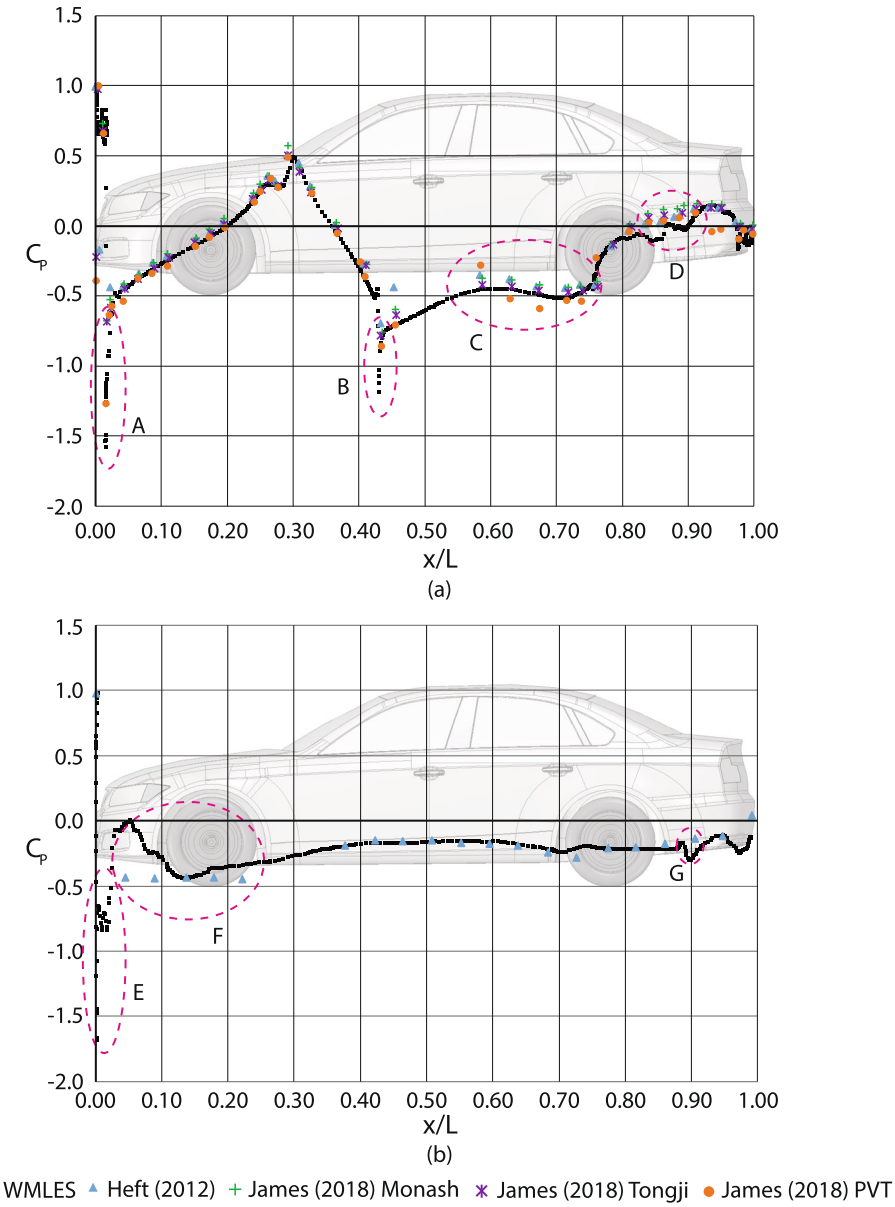

Fig. 7 Pressure coefficients along the center plane of the notchback DrivAer model to compare present WMLES (U_∞ = 15 m/s) with available experimental data (**a**) upperbody and (**b**) underbody

consistent with the numerical results presented. Similarly, an inadequate number of pressure probes near the top of the windshield led to pressure gradients in region B not being captured entirely in experimental studies. In this region, the numerical results also agree more with the experiments conducted at PVT. In region C, the experimental results from PVT deviate the furthest from numerical results and from the results of other wind tunnel experiments. This was noted as a potentially erroneous region at the attachment points of the main body and the interchangeable rear-end [43]. The numerical results deviate slightly from all of the experimental results in region D, which is the rear windshield of the reference model. This region is largely influenced by vortex shedding from the roof,

and the unsteady nature of the flow could have led to the discrepancies observed. Other authors [36, 45] who have used numerical methods have observed inconsistencies in the same regions.

Figure 7(b) shows a plot of the underbody pressure coefficients. The results from James et al. [43] are omitted here because they only conducted surface pressure experiments for a detailed underbody, which is not suitable for comparison with a smooth underbody. There are some large discrepancies seen in regions E and F, which are partially attributed to the low resolution of the wind tunnel results. However, this is a region of complex flow due to the interaction of vortices from the front wheelhouses with the underbody flow near the front bumper. The rest of the pressure measurements in the underbody agree well with the experiment. Region G shows a series of points from the numerical study that appear to capture a minor pressure drop, likely due to the interaction of the underbody flow and the rear-wheel vortices. This was not observed with the experimental results because only a single pressure probe was used in that region.

Figure 8 shows the pressure field of a front and rear wheel, respectively, on the baseline model. A high-pressure region is observed on the front wheel in line with the bottom of the bumper. This area of high pressure is the largest contributor to pressure drag for the wheel. The stagnation region on the front of the wheel causes the incoming underbody flow to accelerate as it yaws past the wheel, creating the low-pressure region observed on the lower outboard side of the wheel. There is evidence of a high-pressure region on the rear wheels, although the pressure observed is much lower than the front-wheel pressure. Therefore, the rear-wheel contribution to the overall pressure drag of the vehicle is much smaller than the front wheel.

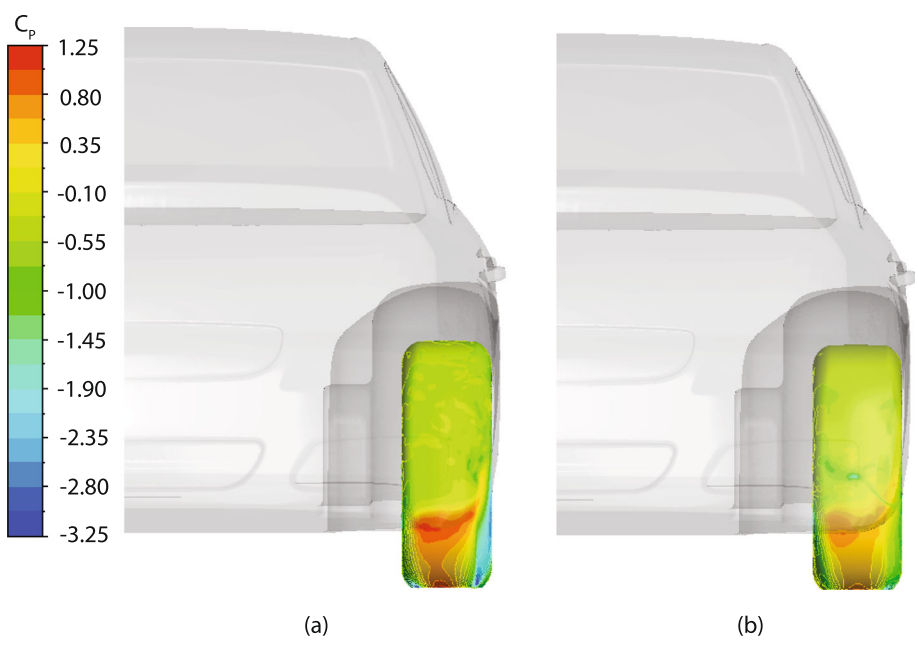

Fig. 8 Pressure coefficient contours for the baseline notchback DrivAer reference model for U_∞ = 15 m/s (**a**) front wheel and (**b**) rear wheel

7 Flow-modification devices

7.1 Conventional wheel deflector

The purpose of the wheel deflector is to reduce the wheel drag and effectively reduce the overall drag experienced by the DrivAer model. However, there is a drag penalty associated with disrupting the underbody flow, and in order to make the wheel deflector effective, the drag penalty must not exceed the drag benefit. Figure 9 shows the drag coefficient of the DrivAer model when fitted with conventional wheel deflectors compared to the baseline model for different freestream speeds. Previous experimental work by [4] and [5] determined that a 40% scale model and a 25% scale model achieve Reynolds independence for the aerodynamic coefficients at approximately Re = 4.2×10^6 and Re = 2.8×10^6, respectively. However, from the present investigation, the full-scale DrivAer model did not achieve Reynolds independence, even at Re = 3.15×10^7 (45 m/s, 100 mph). Therefore, the impact of wheel deflectors on the drag coefficient must be compared separately for each freestream speed considered.

Figure 10 shows the front-wheel drag component for the DrivAer model fitted with conventional wheel deflectors compared to the baseline model. The wheel deflectors prove to be successful in reducing the front-wheel drag—greater front-wheel drag reduction is observed as the height of the wheel deflector is increased. However, the 50-mm wheel deflector, which was particularly effective in [16], produced the greatest drag penalty and increased the overall drag of the DrivAer model by approximately 10% in all cases (Fig. 9). At 45 m/s, the 15-mm wheel deflector caused a drag reduction of 0.25%. All other cases considered resulted in a drag increase, suggesting that the drag penalty of introducing a conventional wheel deflector is detrimental to the aerodynamics of the DrivAer model, even at higher speeds. However, it should be noted that a baseline drag coefficient of 0.231 is relatively low compared to modern sedan cars. Therefore, the shape of the DrivAer model is already favorable from an aerodynamic perspective, and this type of flow-modification device is not appropriate in reducing drag. Additionally, even the

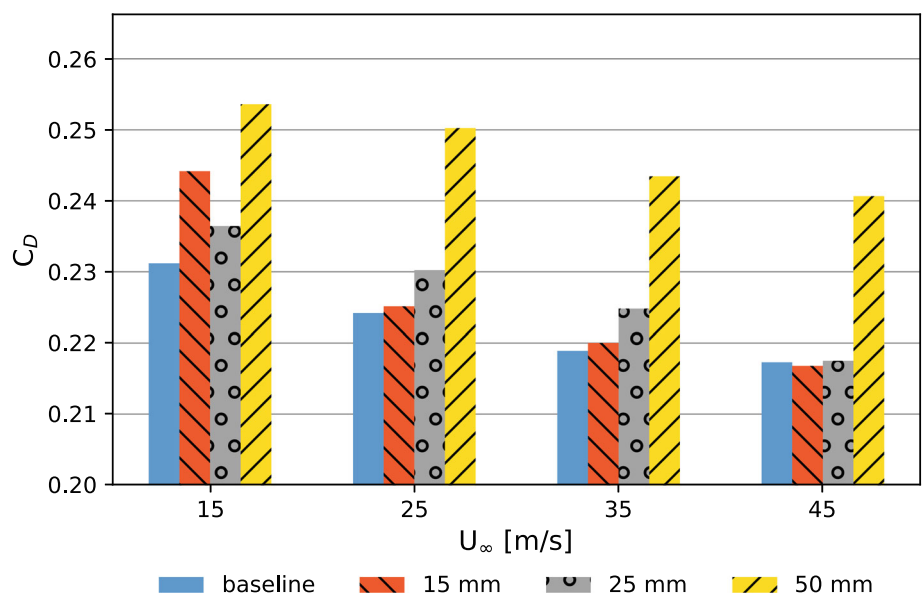

Fig. 9 Time-averaged drag coefficient for the notchback DrivAer model with conventional wheel deflectors

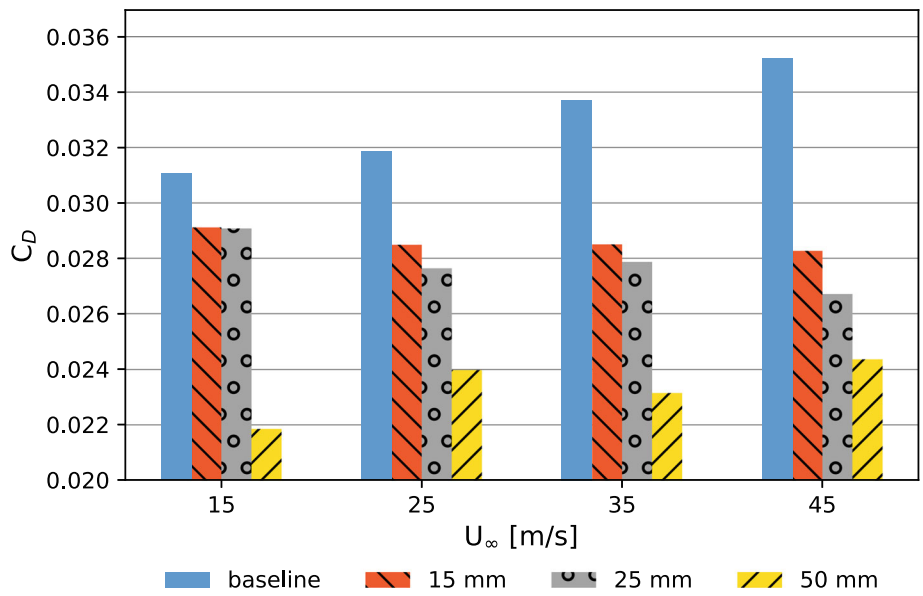

Fig. 10 Time-averaged drag coefficient for the front wheels only with conventional wheel deflectors

15-mm conventional wheel deflector, which was the best performer of the designs considered, would only be beneficial if the vehicle was mostly operating at speeds above 45 m/s (100 mph). At speeds lower than 45 m/s, the conventional wheel deflector has a negative effect on the vehicle drag.

The effect of conventional wheel deflectors on the pressure field of the front wheels was analyzed. Figure 11 shows wheel pressure coefficient contours at a freestream speed of 45 m/s for the baseline model compared to the 15-mm wheel deflector. The top of the high-pressure region on the front wheel follows the shape of the front bumper in the baseline model. The wheel deflector reduces the size of the high-pressure region on the front of the wheel, and the low-pressure region on the side of the wheel, which impacts the flow field in the vicinity of the wheel. However, the wheel deflector, which is attached to the DrivAer body, also experiences a drag force and has a negative impact on the overall drag. Therefore, a reduction in wheel drag does not always lead to a reduction in overall drag.

7.2 90° air-jet wheel deflector

Much like the conventional wheel deflector, the air-jet wheel deflector is intended to divert the flow in the vicinity of the wheel, thereby potentially reducing drag. However, unlike the conventional wheel deflector, the air-jet wheel deflector does not have the associated penalty of having an additional drag-inducing solid surface. The drag coefficient for the baseline DrivAer model with no flow-modification devices is compared to the 90° air-jet wheel-deflector cases in Fig. 12 for four freestream speeds considered.

In all cases, the 90° jets cause a drag penalty that exceeds the drag benefit, resulting in an overall increase in drag force. Figure 13 shows the component of the front-wheel drag that contributes to the total drag for the 90° air-jet wheel deflector cases. In all cases, even though the front-wheel drag is significantly reduced by the wheel deflectors, the body and rear-wheel drag exceeds the baseline case enough to nullify the positive impact of the wheel deflectors. At higher speeds, applying a jet speed of U = 2/3 produces results that

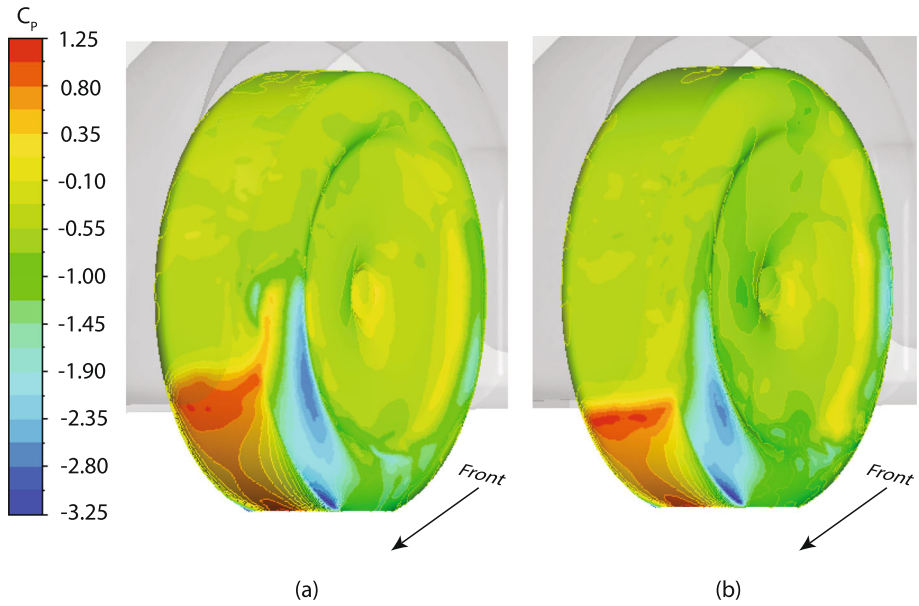

Fig. 11 Pressure coefficient contours on the front left wheel for U_∞ = 45 m/s (a) baseline and (b) 15-mm conventional wheel deflector

are comparable with the baseline, but still present no benefit. Therefore, this jet design is not suitable for overall drag reduction of the DrivAer model in its present configuration. However, it provides an opportunity to study the effects of this technology on the front wheels and underbody flow in order to determine more appropriate flow-modification alternatives for this vehicle model.

Figure 14 shows the front-wheel pressure of the baseline DrivAer model compared to the first air-jet wheel-deflector design, with U = 1/3, 3/3, and 6/3, for a freestream velocity

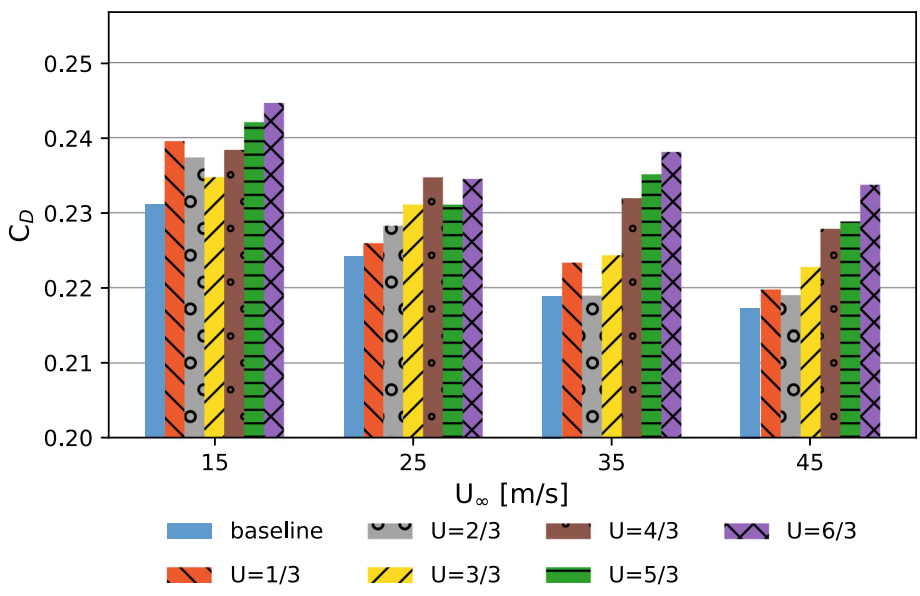

Fig. 12 Time-averaged drag coefficient for the notchback DrivAer model with 90° air-jet wheel deflectors

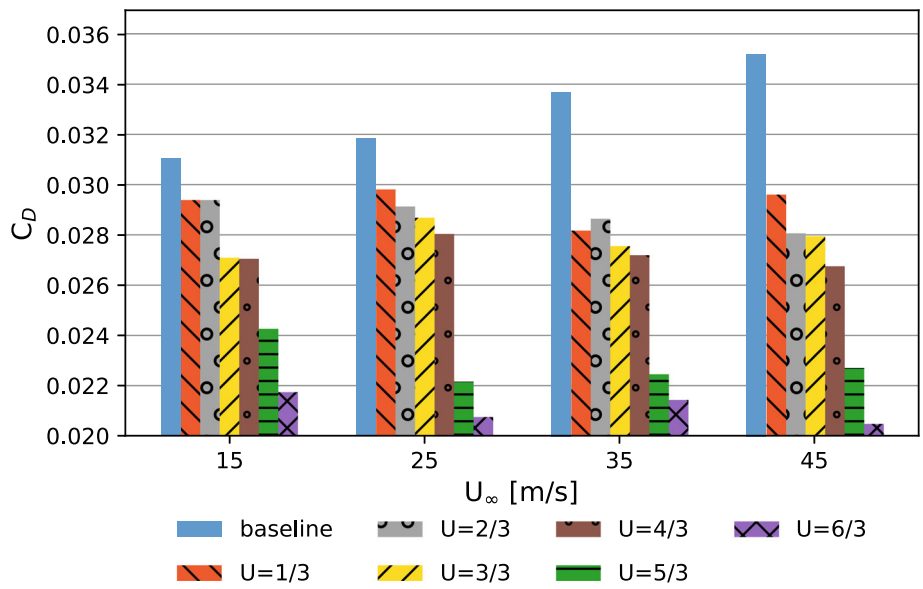

Fig. 13 Time-averaged drag coefficient for the front wheels only with 90° air-jet wheel deflectors

of 15 m/s. The high-pressure region on the front of the wheel diminishes as the air-jet speed is increased. The jet stream causes a momentum change in the underbody flow, pushing it closer to the contact region between the wheel and the ground as the speed of the air jet is increased. Consequently, the high-speed underbody flow impacts a smaller area of the wheel and reduces the wheel drag.

The corresponding bottom view of the DrivAer model, as seen in Fig. 15, shows that as the jet speed is increased, there is evidence of a high-pressure region growing upstream of the air-jet wheel deflectors. This occurs as a result of the incoming underbody flow colliding with the jet stream, thus adding resistance to flow under the vehicle. This provides more evidence that disrupting the underbody flow causes an increase in body drag.

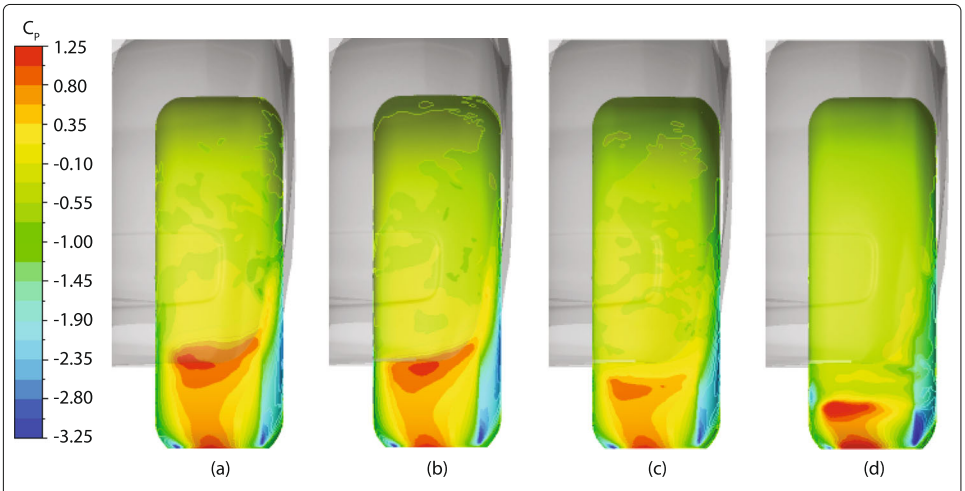

Fig. 14 Pressure coefficient contours on the front left wheel of the notchback DrivAer reference model at U_∞ = 15 m/s (**a**) baseline, (**b**) 90° air jet with U = 1/3, (**c**) 90° air jet with U = 3/3, and (**d**) 90° air jet with U = 6/3

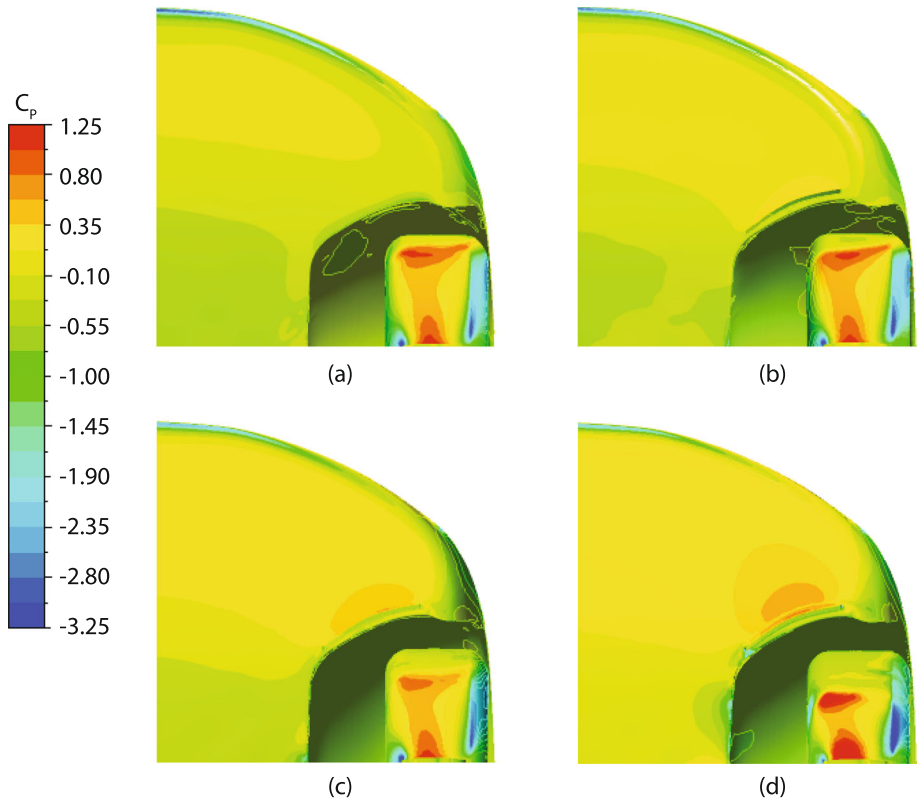

Fig. 15 Pressure coefficient contours on the underside of the front left wheel and surrounding area of the notchback DrivAer reference model at U_∞ = 15 m/s (**a**) baseline, (**b**) 90° air jet with U = 1/3, (**c**) 90° air jet with U = 3/3, and (**d**) 90° air jet with U = 6/3

Figure 16 shows streamlines of the flow approaching the front left wheel for the baseline model, U = 1/3, 3/3, and 6/3 for U_∞ = 15 m/s. In the case of the baseline model, a small portion of the flow is observed to diverge as it enters the wheelhouse region, resulting in a larger impact area of underbody flow on the front wheel. As the speed of the air-jet wheel deflector is increased, the underbody flow is diverted more towards the bottom of the wheel. Although this causes a reduction in the size of the stagnation region, it also causes a local acceleration in the underbody flow, which may lead to higher pressures being observed over a smaller area. This is evident in Fig. 14(d) with the high-pressure contour bands corresponding to 1.025 <C_P <1.25 that are not seen with the lower air-jet speeds.

Dimensionless surface streamlines at a plane 50-mm above the moving ground plane are plotted in Fig. 17. A recirculation region, α, forms in the vicinity of the rear, outboard region of the wheel in the baseline model. This changes the effective shape of the vehicle geometry seen by the incoming airflow. Region α causes underbody flow to yaw away from the vehicle body. After passing region α, the moving air is drawn back towards the underbody, denoted by an arrow labeled β in Fig. 17, and a portion of the flow directly impacts the rear wheel. When air-jet wheel deflectors are introduced, the size of the recirculation region, α, grows proportionally to the speed of the air jets. As region α grows, the yawed flow has a greater tendency to be drawn to the underbody, as seen in Figs. 17(b)

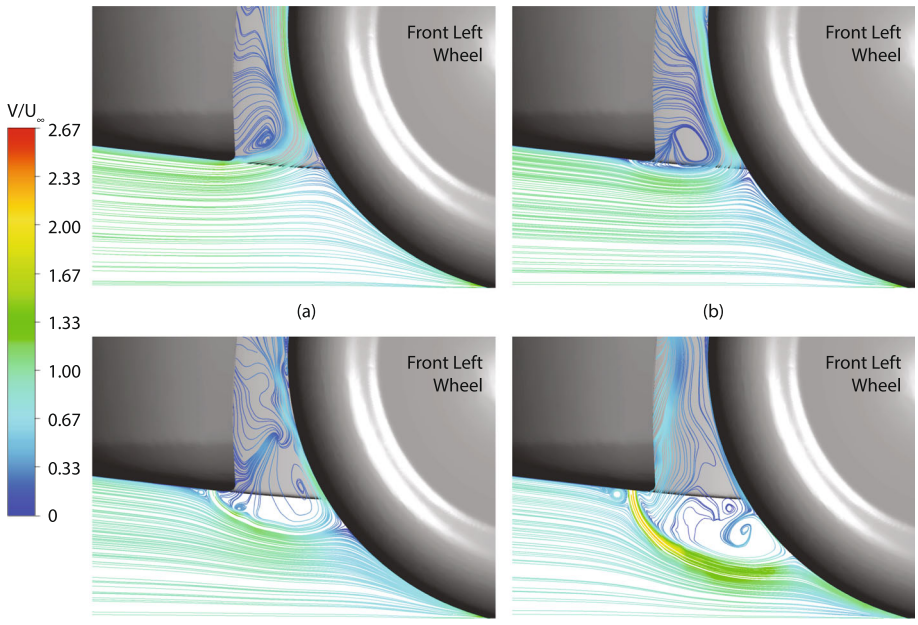

Fig. 16 Streamlines, colored by dimensionless velocity magnitude, approaching the front left wheel of the notchback DrivAer reference model for U_∞ = 15 m/s (**a**) baseline, (**b**) 90° air jet with U = 1/3, (**c**) 90° air jet with U = 3/3, and (**d**) 90° air jet with U = 6/3

and (c). Due to the incident angle of the flow on the rear wheel, the pressure drag experienced by the rear wheel decreases. However, when region α becomes sufficiently large, the suction effect of the underbody causes yawed flow on both sides of car to meet near the midplane and effectively reflect back towards the rear wheels, as shown in Fig. 17(d), causing the rear-wheel drag to increase.

The flow field surrounding a vehicle over a moving ground plane with rotating wheels comprises vortex structures that are revealed by analyzing the velocity gradient tensor. The second invariant of the velocity gradient tensor, Q, represents the local relationship between the shear strain rate and the magnitude of vorticity [46]. Figure 18 shows instantaneous isosurfaces of the second invariant of the velocity gradient tensor corresponding to $Q(D/U_\infty)^2 = 80$. The baseline model shows vortices developing around the wheel as the underbody flow enters and meanders through the wheelhouse. As air-jet wheel deflectors are introduced, and the speed of air injection is increased, the vortex structures around the wheelhouse are observed to decrease. This is most evident when comparing Fig. 18(a), the baseline model, to Fig. 18(b), air-jet wheel deflector with U = 6/3. The flow instability associated with the vortex structures contributes to the drag force experienced by the wheelhouse.

Furthermore, it is evident in Fig. 18 that there are vortex structures forming on either side of the jet streams. The air-jet wheel deflector causes a small recirculation region upstream of the jet which is also seen clearly in Fig. 16(b). This circulation region is responsible for changing the effective shape of the DrivAer model just upstream of the wheelhouse such that the underbody flow can be deflected as intended—the jet stream behaves like an artificial, flexible wall.

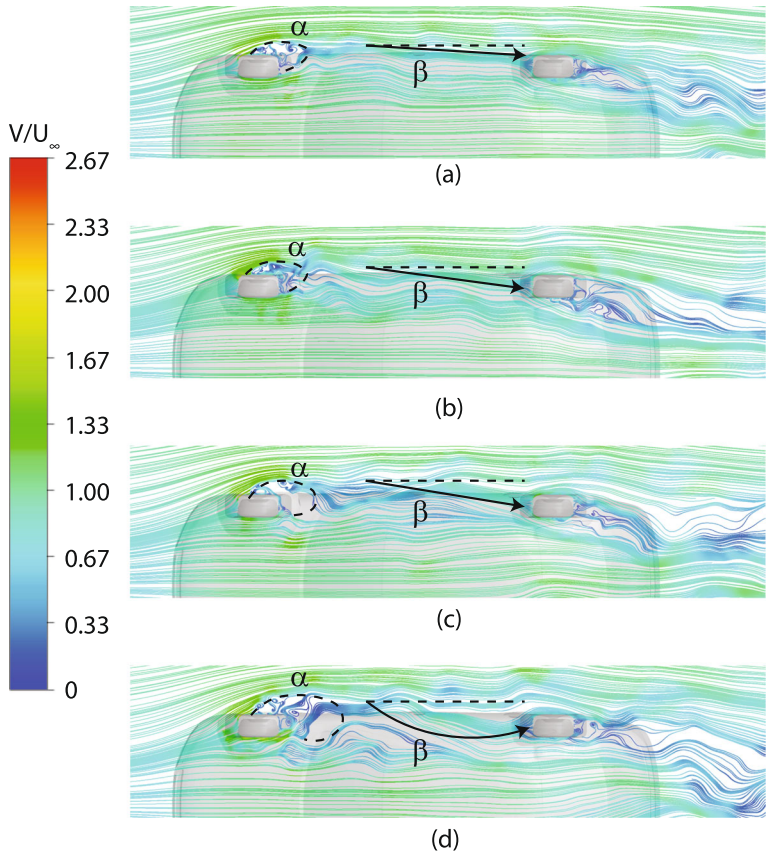

Fig. 17 Surface streamlines, colored by dimensionless velocity magnitude, at z = 50 mm above the ground plane for U_∞ = 15 m/s (**a**) baseline, (**b**) 90° air jet with U = 1/3, (**c**) 90° air jet with U = 3/3, and (**d**) 90° air jet with U = 6/3

7.3 45° air-jet wheel deflector

In order to have a net-positive effect, the jet stream from the wheel deflector has to mix smoothly with the underbody flow. The angled air-jet wheel deflector has a velocity component parallel to the underbody flow but still achieves flow deflection such that the stagnation region is diminished. Figure 19 shows the drag coefficient for the 45° air-jet

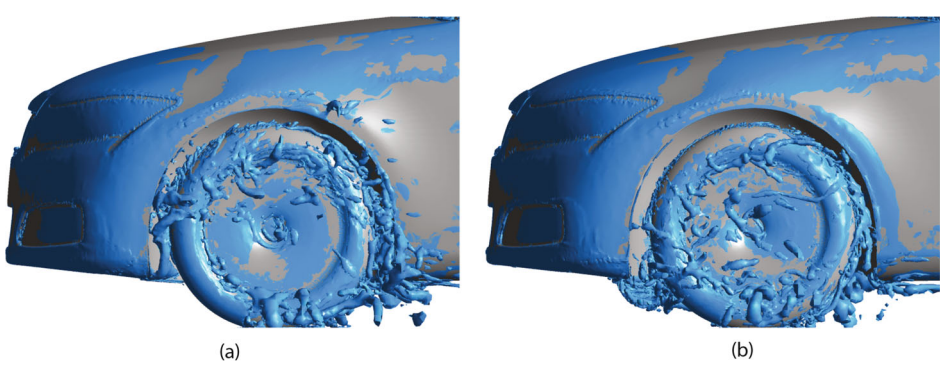

Fig. 18 Isosurfaces of the second invariant velocity gradient tensor, $Q(D/U_\infty)^2 = 80$, for U_∞ = 15 m/s (**a**) baseline, (**b**) 90° air jet with U = 6/3

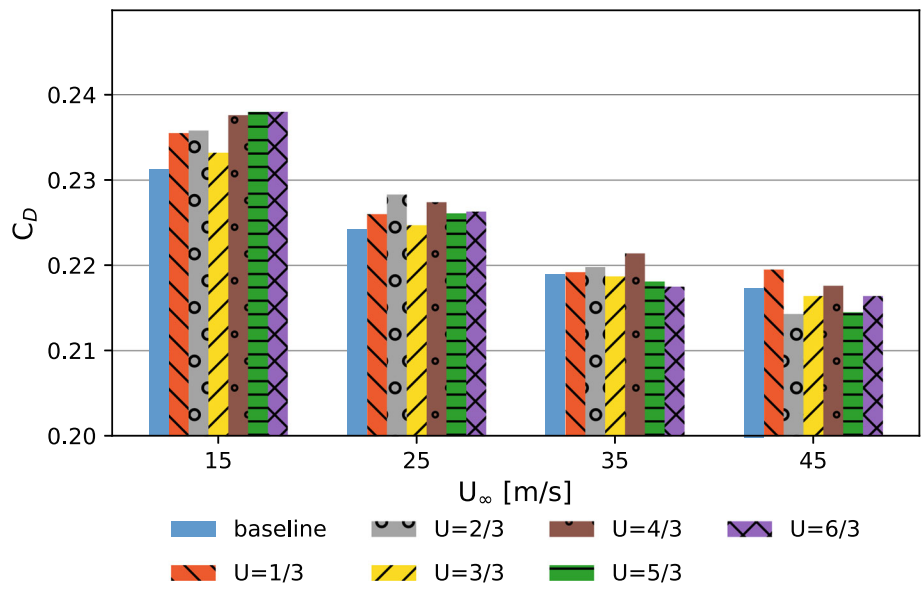

Fig. 19 Time-averaged drag coefficient for the notchback DrivAer model with 45° air-jet wheel deflectors

wheel deflector for four freestream speeds investigated. At inlet speeds of 15 m/s and 25 m/s, the overall drag of the DrivAer model with air jets is observed to be greater than the baseline model. At higher speeds, the aerodynamic drag dominates, and the air-jet wheel deflectors have a greater impact.

Comparing the 90° and 45° air-jet wheel deflector designs, it is clear that the latter had more of an impact on overall drag reduction. The 45° air-jet wheel deflector successfully reduced the drag below the baseline value for some cases at 35 and 45 m/s freestream speeds. At 35 m/s, a drag reduction of up to 0.65% is observed when a jet speed of 70 m/s (U = 6/3) is applied. At 45 m/s, a drag reduction of 1.4% is observed with a jet speed of 30 m/s (U = 2/3). Due to the interaction of flow structures of different frequencies, the drag coefficient does not decrease linearly with increasing jet speed.

Figure 20 shows wheel surface pressure contours and streamlines originating from the left jet for the 90° and 45° air-jet wheel deflectors with a jet speed of U=2/3 for a freestream speed of 45 m/s. The 45° jets appear more flattened by the underbody flow and consequently do not reduce the high pressure region as much as the 90° jets—hence, the greater wheel drag reduction for the 90° jet. However, due to the reduced angle, the 45° jet leads to better mixing and still plays an important role in ensuring the underbody flow does not expand when it reaches the wheelhouse, thus reducing the flow impact area on the wheels compared to the baseline case and reducing the wheel drag sufficiently to result in an overall drag reduction for this case.

The front-wheel drag is successfully reduced by the air-jet wheel deflectors for all cases as shown in Fig. 21. The greatest impact of the air jets on the front wheels is observed at a freestream speed of 15 m/s. However, at low speed, the contribution of the front wheels on the vehicle drag is too small to have a positive impact. At a freestream speed of 45 m/s, the greatest reductions to front wheel drag occur when U = 2/3 and U = 5/3. As seen in Fig. 19, this translates to a reduction in overall vehicle drag.

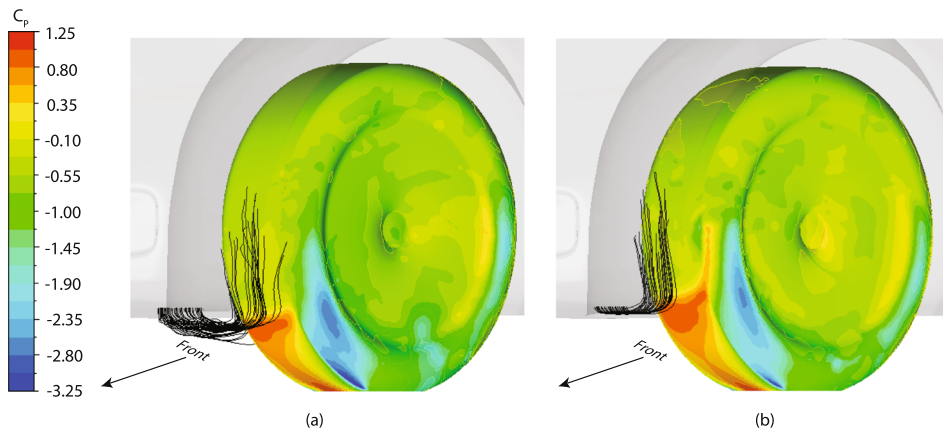

Fig. 20 Pressure coefficient contour diagram for the notchback DrivAer model for U_∞ = 45 m/s with U = 2/3 (**a**) 90° air-jet wheel deflector (**b**) 45° air-jet wheel deflector

The 45° wheel deflectors were more successful because of the smaller effect on the underbody flow further from the wheelhouse region. This is observed when comparing the drag components for the 90° air-jet cases from Fig. 13 to the 45° air-jet cases presented in Fig. 21. Figure 13 shows that for a freestream of 45 m/s, a jet speed of U=2/3 for the 90° air-jet wheel deflector reduced the front-wheel drag by 21.3%, while the 45° air jet results in a 14.1% drag reduction (Fig. 21). However, the former results in a 5% increase in body drag (DrivAer body only without front and rear wheels), while the latter only leads to a 1% increase —recall that the body-drag contribution is much larger than the wheel drag.

Finally, since some of the air-jet configurations for 45° show promise for higher air speeds, the effect of the jets on lift is examined. The lift coefficients for the 45° air-jet case are presented in Fig. 22. The case with the greatest overall drag reduction (U = 2/3 at 45 m/s) of up to 1.5% when compared to the baseline model shows a change in lift

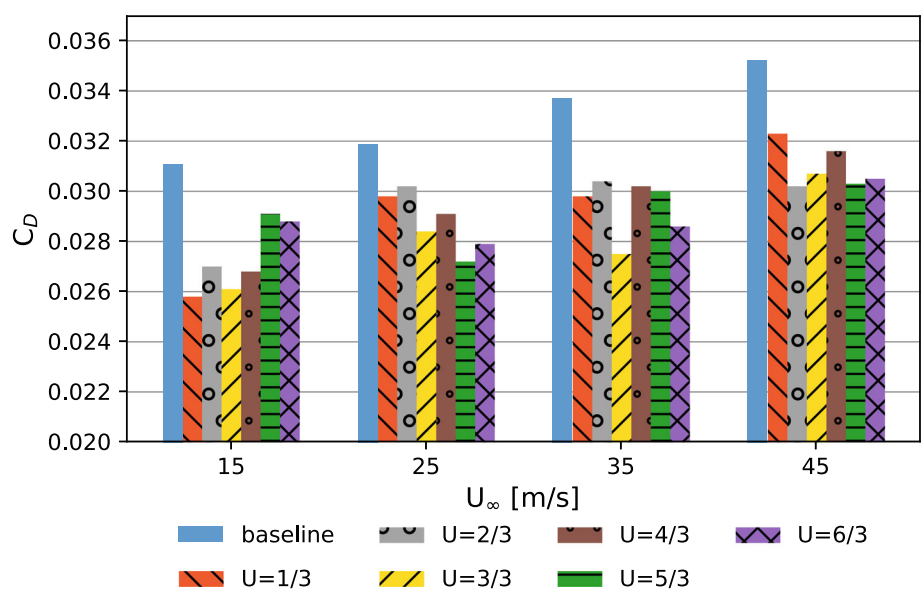

Fig. 21 Time-averaged drag coefficient for the front wheels only with 45° air-jet wheel deflectors

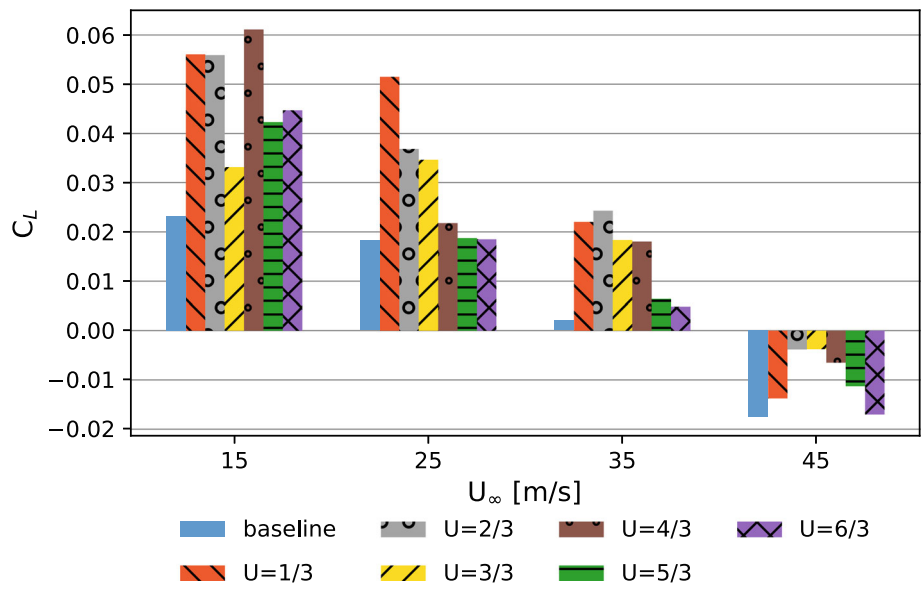

Fig. 22 Time-averaged lift coefficient for the notchback DrivAer model with 45° air-jet wheel deflectors

coefficient of 1.2%. In all cases (including the lift coefficients for the conventional and 90° air-jet wheel deflectors), the introduction of the flow-modification devices had a net increase in positive lift. Even when the baseline model exhibits a downforce at 45 m/s, the subsequent air-jet cases reveal a reduction in downforce, showing that the air jets are contributing a lift force to the vehicle. It should be noted that the lift coefficients are very small compared to the drag coefficients, so their effect on typical passenger vehicles, including the DrivAer model, is not as important.

8 Concluding remarks

The DrivAer model is based on two production passenger cars—the 3 Series BMW and the Audi A4. The particular configuration presented here lacks some of the details that the production cars have: no detailed underbody, no mirrors, and no rims. Therefore, the drag coefficients reported are lower than they would be in most practical situations. However, this study presents valuable insight on the impact of wheel deflectors on the drag force experienced by modern sedan cars. Particularly, conventional wheel deflectors can have a negative impact on vehicle drag, even at high speeds, for vehicles that are already relatively streamlined. Additionally, cars are becoming increasingly aerodynamic with time, and design features that were once believed to be beneficial need to be reassessed. Perhaps traditional flow-control methods are more beneficial for larger vehicles that experience greater drag forces and have more ground clearance. For example, the Nissan Qashqai, which has a drag coefficient approximately 30% greater than the DrivAer model studied here, seems to benefit significantly from the presence of conventional wheel deflectors [17].

At higher speeds, the resistance to motion for ground vehicles is dominated by aerodynamic drag; at lower speeds, rolling resistance is the dominant force. Therefore, a reduction in aerodynamic drag at lower speeds has less of an impact on the overall drag than at higher speeds. Two different flow-modification devices were applied to the

notchback DrivAer model, and it was determined that when a freestream speed of 15 m/s was applied, the drag penalty associated with modifying the DrivAer flow field exceeds the drag benefit with both devices. However, at higher speeds, both devices become more effective. Additionally, a reduction in wheel drag did not always result in an overall drag reduction. Due to the competing effects of disrupting underbody flow and altering the stagnation region on the wheels, there is a balance required in order to achieve an overall reduction in drag.

Most countries have speed limits that restrict the legal operation of vehicles to speeds less than 70 mph. Therefore, using a conventional wheel deflector that is only beneficial at speeds above 45 m/s (100 mph) is impractical. Instead, it would be beneficial to implement a flow-modification device that can be turned off at lower speeds. However, it should also be noted that the flow-modification devices presented here would likely have a more significant impact on vehicles that have a greater baseline drag coefficient. Furthermore, there is potential for the air-jet wheel deflector to be much more beneficial on the notchback DrivAer model than observed from the current investigation. The model used in these simulations had a smooth underbody to save on computational cost, resulting in less tumultuous flow under the vehicle body. Wind tunnel experiments conducted by Heft et al. [4] showed that a detailed underbody adds C_D=0.03 to the overall drag of the 40% scale DrivAer model. Simulating a detailed underbody will provide further insight on the flow field and more context to the real-life practicality of this technology. Future work on this topic should also include a detailed rim. Although it will require more computational time due to time-dependent remeshing, and a moving reference frame for the wheel tread, the benefit is a more comprehensive understanding of flow-modification devices on the flow field near the wheel when the fan effect caused by the spokes is present [15].

Disparities are observed between results obtained using a steady and unsteady formulation for the DrivAer reference model. This occurs due to the fact that the surrounding flow field is characterized by several time-dependent vortex structures that are not captured by steady-state formulation. Therefore, in order to accurately represent the flow field around the DrivAer model, and capture the unsteadiness, it is necessary to use flow-resolving methods such as LES and DES. However, such methods require greater computational resources than RANS. The baseline DrivAer model simulated using WMLES with the coarse mesh took approximately 21 hours with 360 Linux processors. IDDES cases required, on average, 58% more computation time than WMLES cases—a significant amount of time considering the resources required for computation. IDDES results were found to be less accurate than WMLES results when compared to experimental data for the coarse and medium meshes. A relatively small difference was observed applying IDDES with the fine mesh, but the computational time required to achieve this result was 169% greater than with WMLES with the coarse mesh, which yielded comparable results. Therefore, in order to achieve more accurate time-averaged force coefficients with a shorter computation time, WMLES is recommended over IDDES.

The consideration of aesthetics is important in vehicle design. Many customers who purchase cars consider the appearance as well as the utility. Air-jet wheel deflectors will potentially present drag-reduction opportunities without any visible modification to the vehicle exterior. Even though conventional wheel deflectors are a minute feature of

passenger cars, there is potential to eliminate them altogether while still achieving the intended effect of underbody flow deflection.

The inclusion of air-jet wheel deflectors has additional implications. The present investigation shows the underhood as a blackbox, but in reality, there will either need to be mechanical components added to compress the underhood air and discharge it at the desired location, or the underhood will need to be designed to release just upstream of the front wheels—many automotive manufacturers presently purge underhood flow through the underbody or the wheelhouse. The inclusion of mechanical components can be costly and will add to the weight of the vehicle, but will provide an opportunity to control the jet speed as needed. The case where underhood air is intentionally directed to release upstream of the front wheels forms a passive system. This passive flow modification will lead to a constant jet-to-freestream speed relationship. However, a system like this will need to be turned off at lower speeds where flow modification is undesirable.

Acknowledgments
The authors gratefully acknowledge Embry-Riddle Aeronautical University for providing computing time on the Vega supercomputer.

Authors' contributions
KLN: Conceptualization; Methodology; Software; Validation; Investigation; Formal analysis; Writing—original draft; Writing—review and editing. SKSB: Conceptualization; Writing—review and editing; Supervision. The authors read and approved the final manuscript.

Funding
Not applicable.

Availability of data and materials
The datasets used and/or analysed during the current study are available from the corresponding author on reasonable request.

Declarations

Competing interests
The authors declare that they have no competing interests.

Received: 13 July 2021 Accepted: 26 August 2021
Published online: 01 October 2021

References

1. Le Good GM, Garry KP (2004) On the use of reference models in automotive aerodynamics. In: SAE Technical Paper Series. SAE International. https://doi.org/10.4271/2004-01-1308
2. Ahmed SR, Ramm G, Faltin G (1984) Some salient features of the time-averaged ground vehicle wake. In: SAE Technical Paper Series. SAE International. https://doi.org/10.4271/840300
3. Cogotti A (1998) A parametric study on the ground effect of a simplified car model. In: SAE Technical Paper Series. SAE International. https://doi.org/10.4271/980031
4. Heft AI, Indinger T, Adams NA (2012) Introduction of a new realistic generic car model for aerodynamic investigations. In: SAE Technical Paper Series. SAE International. https://doi.org/10.4271/2012-01-0168
5. Strangfeld C, Wieser D, Schmidt H-J, Woszidlo R, Nayeri C, Paschereit C (2013) Experimental study of baseline flow characteristics for the realistic car model DrivAer. In: SAE Technical Paper Series. SAE International. https://doi.org/10.4271/2013-01-1251
6. Wieser D, Schmidt H-J, Müller S, Strangfeld C, Nayeri C, Paschereit C (2014) Experimental comparison of the aerodynamic behavior of fastback and notchback DrivAer models. SAE Int J Passenger Cars - Mech Syst 7(2):682–691. https://doi.org/10.4271/2014-01-0613
7. Wieser D, Nayeri C, Paschereit CO (2015) Experiments with vortex generators applied to a notchback car model. In: 53rd AIAA Aerospace Sciences Meeting. American Institute of Aeronautics and Astronautics, Kissimmee. https://doi.org/10.2514/6.2015-1236
8. Pujals G, Depardon S, Cossu C (2010) Drag reduction of a 3D bluff body using coherent streamwise streaks. Exp Fluids 49(5):1085–1094. https://doi.org/10.1007/s00348-010-0857-5
9. Steinfurth B, Berthold A, Feldhus S, Haucke F, Weiss J (2019) Increasing the aerodynamic performance of a formula student race car by means of active flow control. In: SAE Technical Paper Series. SAE International. https://doi.org/10.4271/2019-01-0652

10. Tandon R, Agrewale MR, Vora K (2019) Aerodynamic analysis of a passenger car to reduce drag using active grill shutter and active air dam. In: SAE Technical Paper Series. SAE International. https://doi.org/10.4271/2019-28-2408
11. Kurec K, Remer M, Mayer T, Tudruj S, Piechna J (2019) Flow control for a car-mounted rear wing. Int J Mech Sci 152:384–399. https://doi.org/10.1016/j.ijmecsci.2018.12.034
12. Nath DS, Pujari PC, Jain A, Rastogi V (2021) Drag reduction by application of aerodynamic devices in a race car. Adv Aerodyn 3(1):4. https://doi.org/10.1186/s42774-020-00054-7
13. Hucho WH (1998) Aerodynamics of road vehicles. 4th edn. SAE International, Warrendale
14. Hucho W, Sovran G (1993) Aerodynamics of road vehicles. Ann Rev Fluid Mech 25(1):485–537. https://doi.org/10.1146/annurev.fl.25.010193.002413
15. Wickern G, Zwicker K, Pfadenhauer M (1997) Rotating wheels - their impact on wind tunnel test techniques and on vehicle drag results. In: SAE International Congress and Exposition. SAE International. https://doi.org/10.4271/970133
16. Sebben S (2004) Numerical simulations of a car underbody: Effect of front-wheel deflectors. SAE Tech Pap. https://doi.org/10.4271/2004-01-1307
17. Kremheller A (2014) The aerodynamics development of the new Nissan Qashqai. In: SAE Technical Paper Series. SAE International. https://doi.org/10.4271/2014-01-0572
18. Brunn A, Nitsche W (2006) Active control of turbulent separated flows over slanted surfaces. Int J Heat Fluid Flow 27(5):748–755. https://doi.org/10.1016/j.ijheatfluidflow.2006.03.006
19. Littlewood RP, Passmore MA (2012) Aerodynamic drag reduction of a simplified squareback vehicle using steady blowing. Exp Fluids 53(2):519–529. https://doi.org/10.1007/s00348-012-1306-4
20. Joseph P, Amandolèse X, Aider J-L (2011) Drag reduction on the 25° slant angle Ahmed reference body using pulsed jets. Exp Fluids 52(5):1169–1185. https://doi.org/10.1007/s00348-011-1245-5
21. McNally J, Mazellier N, Alvi F, Kourta A (2019) Control of salient flow features in the wake of a 25 deg. Ahmed model using microjets. Exp Fluids 60(1):7. https://doi.org/10.1007/s00348-018-2645-6
22. Barsotti DL, Divo EA, Boetcher SKS (2015) Optimizing jets for active control of wake refinement for ground vehicles. J Fluids Eng 137(12):121108. https://doi.org/10.1115/1.4030913
23. Wang BX, Yang ZG, Zhu H (2019) Active flow control on the 25° Ahmed body using a new unsteady jet. Int J Heat Fluid Flow 79:108459. https://doi.org/10.1016/j.ijheatfluidflow.2019.108459
24. Baek S-W, Lee SW (2019) Aerodynamic drag reduction on a realistic vehicle using continuous blowing. Microsyst Technol 26(1):11–23. https://doi.org/10.1007/s00542-019-04355-w
25. Wieser D, Lang H, Nayeri C, Paschereit C (2015) Manipulation of the aerodynamic behavior of the DrivAer model with fluidic oscillators. SAE Int J Passenger Cars - Mech Syst 8(2):687–702. https://doi.org/10.4271/2015-01-1540
26. Fabijanic J (1996) An experimental investigation of wheel-well flows. In: SAE Technical Paper Series. SAE International. https://doi.org/10.4271/960901
27. Lee SW (2018) Computational analysis of air jet wheel deflector for aerodynamic drag reduction of road vehicle. Microsyst Technol 24(11):1–11. https://doi.org/10.1007/s00542-018-3992-1
28. Nabutola KL, Boetcher SKS (2019) Drag reduction of ground vehicles using air-injected wheel deflectors. In: Proceedings of the ASME 2019 International Mechanical Engineering Congress & Exposition. https://doi.org/10.1115/IMECE2019-10454
29. Menter FR (1994) Two-equation eddy-viscosity turbulence models for engineering applications. AIAA J 32(8):1598–1605. https://doi.org/10.2514/3.12149
30. Menter F, Kuntz M, Langtry R (2003) Ten years of industrial experience with the SST turbulence model. In: Proceedings of the 4th International Symposium on Turbulence, Heat and Mass Transfer. Begell House Inc., West Redding Vol. 4. pp 625–632
31. Heft A, Indinger T, Adams N (2011) Investigation of unsteady flow structures in the wake of a realistic generic car model. In: 29th AIAA Applied Aerodynamics Conference. American Institute of Aeronautics and Astronautics. https://doi.org/10.2514/6.2011-3669
32. Menter F, Kuntz M, Bender R (2003) A scale-adaptive simulation model for turbulent flow predictions. In: 41st Aerospace Sciences Meeting and Exhibit. American Institute of Aeronautics and Astronautics. https://doi.org/10.2514/6.2003-767
33. Ashton N, Revell A (2015) Comparison of RANS and DES methods for the DrivAer automotive body. In: SAE Technical Paper Series. SAE International. https://doi.org/10.4271/2015-01-1538
34. Cho J, Park J, Yee K, Kim H-L (2018) Comparison of various drag reduction devices and their aerodynamic effects on the DrivAer model. SAE Int J Passenger Cars - Mech Syst 11(3):225–238. https://doi.org/10.4271/06-11-03-0019
35. Shur ML, Spalart PR, Strelets MK, Travin AK (2008) A hybrid RANS-LES approach with delayed-DES and wall-modelled LES capabilities. Int J Heat Fluid Flow 29(6):1638–1649. https://doi.org/10.1016/j.ijheatfluidflow.2008.07.001
36. Aljure DE, Calafell J, Baez A, Oliva A (2018) Flow over a realistic car model: Wall modeled large eddy simulations assessment and unsteady effects. J Wind Eng Ind Aerodyn 174:225–240. https://doi.org/10.1016/j.jweia.2017.12.027
37. Collin C, Mack S, Indinger T, Mueller J (2016) A numerical and experimental evaluation of open jet wind tunnel interferences using the DrivAer reference model. SAE Int J Passenger Cars - Mech Syst 9(2):657–679. https://doi.org/10.4271/2016-01-1597
38. Krajnović S, Sarmast S, Basara B (2011) Numerical investigation of the flow around a simplified wheel in a wheelhouse. J Fluids Eng, Trans ASME 133(11):111001. https://doi.org/10.1115/1.4004992
39. Nabutola KL, Boetcher SKS (2021) On the validation of turbulence models for wheel and wheelhouse aerodynamics. J Verification, Validation Uncertain Quantif 6(2):021006. https://doi.org/10.1115/1.4050611
40. Davidson L (2009) Large eddy simulations: How to evaluate resolution. Int J Heat Fluid Flow 30(5):1016–1025. https://doi.org/10.1016/j.ijheatfluidflow.2009.06.006
41. Ekman P, Larsson T, Virdung T, Karlsson M (2019) Accuracy and speed for scale-resolving simulations of the DrivAer reference model. In: SAE Technical Paper Series. SAE International. https://doi.org/10.4271/2019-01-0639
42. Soares RF, de Souza FJ (2015) Influence of CFD setup and brief analysis of flow over a 3D realistic car model. In: SAE Technical Paper Series. SAE International. https://doi.org/10.4271/2015-36-0513

43. James T, Krueger L, Lentzen M, Woodiga S, Chalupa K, Hupertz B, Lewington N (2018) Development and initial testing of a full-scale DrivAer generic realistic wind tunnel correlation and calibration model. SAE Int J Passenger Cars - Mech Syst 11(5):353–367. https://doi.org/10.4271/2018-01-0731
44. Ljungskog E, Sebben S, Broniewicz A (2020) Inclusion of the physical wind tunnel in vehicle CFD simulations for improved prediction quality. J Wind Eng Ind Aerodyn 197:104055. https://doi.org/10.1016/j.jweia.2019.104055
45. Guilmineau E (2014) Numerical simulations of ground simulation for a realistic generic car model. In: Volume 1C, Symposia: Fundamental Issues and Perspectives in Fluid Mechanics Industrial and Environmental Applications of Fluid Mechanics Issues and Perspectives in Automotive Flows Gas-Solid Flows. American Society of Mechanical Engineers. https://doi.org/10.1115/fedsm2014-21164
46. Jeong J, Hussain F (1995) On the identification of a vortex. J Fluid Mech 285:69–94. https://doi.org/10.1017/s0022112095000462

Publisher's Note

Springer Nature remains neutral with regard to jurisdictional claims in published maps and institutional affiliations.

Ready to submit your research? Choose BMC and benefit from:

- fast, convenient online submission
- thorough peer review by experienced researchers in your field
- rapid publication on acceptance
- support for research data, including large and complex data types
- gold Open Access which fosters wider collaboration and increased citations
- maximum visibility for your research: over 100M website views per year

At BMC, research is always in progress.

Learn more biomedcentral.com/submissions

BMC